

## Confinement and fuelling in MAST

M. Valovič, L. Garzotti, S. Saarelma, A. Thyagaraja, R. Akers, G. Cunningham, A. Patel, D. Muir, M. Turnyanskiy, M. Walsh and the MAST team

EURATOM/UKAEA Fusion Association, Culham Science Centre, Abingdon, Oxon OX14 3DB, UK

e-mail contact of main author: martin.valovic@ukaea.org.uk

**Abstract.** The dependencies of energy confinement on the main engineering parameters have been investigated in the Mega Ampere Spherical Tokamak (MAST) in H-mode by expanding operational space towards higher plasma currents (up to 1.2MA) and heating powers (up to 3.5MW). Multivariate fits show that the dependence of energy confinement time on plasma current  $I_p$  is weaker than linear while the dependence on toroidal magnetic field  $B_T$  is stronger than linear, in contrast to conventional energy confinement scalings. These  $I_p$  and  $B_T$  dependencies have also been confirmed by single parameter scans. Transport analysis indicates that the strong  $B_T$  scaling of energy confinement could possibly be explained by weaker  $q$  and stronger  $v^*$  dependence of heat diffusivity. Particle confinement has been studied using shallow high field side pellets. The pellet deposition can be explained only by invoking the grad-B drift of the pellet ablatant. The pellet creates a distinct zone with sharp positive density gradient and doubled temperature gradient. Simulations using the linear GS2 and CUTIE codes show that these changes could modify the character of micro-turbulence in the pellet deposition zone. The pellet retention time scales with energy confinement time and increases with pellet deposition depth. Energy and particle confinement scalings derived from MAST data are used for prediction towards a Component Test Facility based on the spherical tokamak (ST-CTF). The energy confinement time scaling gives about  $\sim 1.6$  more favourable prediction than the IPB98(y,2) scaling, however, the strong  $B_T$  dependence in STs has yet to be tested towards the low  $v^*$  of a ST-CTF. The scaling for particle confinement predicts that for ST-CTF pellet particle throughput should be about 20 Pa m<sup>3</sup>/s, which is 1/4 of the value predicted by the same scaling for ITER.

### 1. Introduction

Energy and particle confinement scalings play a central role in design of tokamak fusion reactors. Conventional energy confinement scalings such as IPB98(y,2) [1] display strong (linear) dependence on plasma current. As a result plasma current is the main driver in design of conventional aspect ratio fusion reactors [2, 3]. Fusion reactors based on low aspect ratio tokamaks have been so far designed using the confinement scaling derived on conventional tokamaks [4]. This has some support from the fact that the values of energy confinement in low aspect ratio tokamaks MAST and NSTX broadly agree with those predicted by the conventional energy confinement scaling IPB98(y,2) [5, 6]. Nevertheless the parametric dependencies of energy confinement in low aspect ratio tokamaks differ from IPB98(y,2) scaling. Favourable collisionality dependence was found in MAST [5] and NSTX data [7] and linear dependence on toroidal magnetic field was reported in NSTX [8].

Particle confinement drives the design of fuelling systems. The present consensus is that in reactor grade plasmas the most promising fuelling technique is the injection of cryogenic pellets [9, 10]. Particle confinement scalings are not so well developed as their energy confinement counterparts and even less is known for conditions with pellet fuelling. The analysis could be simplified by the fact that the particle confinement is linked to energy confinement as they are both dominated by anomalous transport in the outer part of the plasma. On the other hand it also means that the modification of density and temperature profiles by pellets may affect the energy confinement itself.

The first part of this paper deals with the energy confinement scaling, in particularly with plasma current and toroidal magnetic field dependencies. The second part reports on the particle confinement studies using pellet fuelling. For more details see [11].

## 2. Energy confinement in H-mode

The dataset used for this study expands significantly the parameter range in comparison with our most recent publication [5], in particular towards higher heating powers and higher plasma current. The data consist of ELMy and ELM-free H-mode plasmas with double null divertor configuration. The engineering parameters span the following intervals: plasma current  $I_p = (0.60 - 1.17)MA$ , geometric major radius  $R_{geo} = (0.77 - 0.90)m$ , minor radius  $a = (0.54 - 0.62)m$ , elongation  $\kappa = 1.7 - 2.0$ , triangularity  $\delta = 0.4 - 0.5$ , vacuum toroidal field at the geometric radius  $B_T = (0.34 - 0.50)T$  and line averaged density  $\bar{n}_e = (2.1 - 5.4) \times 10^{19} m^{-3}$ . The working gas is deuterium and plasmas are heated with neutral beams with injected power of  $P_{INJ} = (1.2 - 3.5)MW$  with energy of  $\leq 65 - 67 keV$ . Sawteeth are avoided by an application of neutral beam heating during current ramp-up. This is different from majority of data in conventional multi-machine database which is dominated by sawtoothing plasmas [1]. Data are extracted at times close to the flat top of energy content. Only one data point per shot is taken.

Figure 1 shows the ordinary least square regression fit (OLS) to the total energy content  $W_{mag} = C I_p^{\alpha_I} B_T^{\alpha_B} \bar{n}_e^{\alpha_n} P_L^{\alpha_P}$ . Here,  $W_{mag}$  is the energy content from equilibrium reconstruction (EFIT) and  $P_L = P_{ohm} + P_{INJ} - dW_{mag}/dt$  is the power loss where  $P_{ohm}$  is the ohmic power,  $P_{INJ}$  is the injected beam power. Beam shine through and unconfined orbit losses, calculated for representative shots by the TRANSP code [12], are a few percent [5] and are neglected in this part of the analysis. Radiated power ( $<13\%$  of  $P_L$ ) is not included in confinement scaling laws by convention [1]. The exponents obtained are given in table 1, case 1. It is seen that the scaling shows much stronger dependence on toroidal magnetic field than the IPB98(y,2) scaling while the scaling with plasma current is weaker. It is well known that OLS regression can give biased results if independent variables have errors comparable with error of dependent variable. This is clearly our case where the errors are estimated as  $\delta I_p = 1\%$ ,  $\delta B_T = 1.5\%$ ,  $\delta \bar{n}_e = 7\%$ ,  $\delta P_L = 10\%$ ,  $\delta W_{mag} = 10\%$ . This problem is dealt with by using the principal component analysis and error-in-variable method (PCEIV) [13, 14]. In this technique all variables, including energy content, are put into a single set and the logarithms of all variables are weighted by an inverse of their relative errors. Then the exponents in the scaling are found from the coefficients corresponding to the principal component having the smallest variation. The result of such a

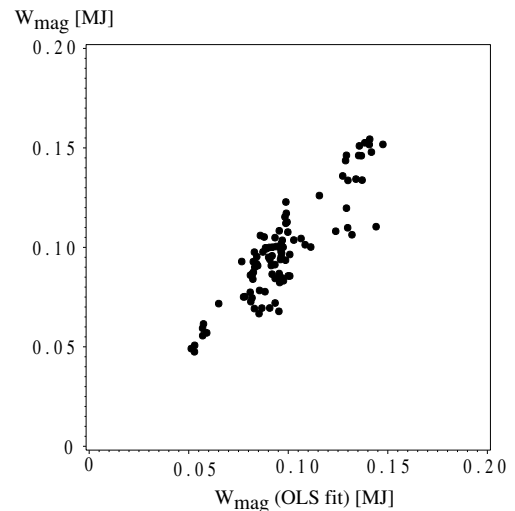


FIG 1. Regression analysis to total energy content (exponents are in table 1, case 1).

Table 1. Summary of energy confinement scalings. Units are MJ, MA, T,  $10^{19} m^{-3}$  and MW.

case	method	$C$	$\alpha_I$	$\alpha_B$	$\alpha_n$	$\alpha_P$	N	RMSE %
1	OLS	0.252	0.59	1.4	0.00	0.27	97	12.1
2	PCEIV	-	0.51	1.6	-0.06	0.39	97	-
3	IPB98(y,2) [1]	0.0562	0.93	0.15	0.41	0.31	-	14.5

fitting procedure is shown in table 1, case 2. It is seen however, in this case, that the PCEIV method gives rather similar results to the OLS regression. The differences are in the range predicted by a principal component analysis (PCA) given in the next paragraph.

Another common problem with multivariate fits is that datasets are not well conditioned to extract all exponents due to the correlations between variables. To assess the conditions in our database, a PCA on a set  $(I_p, B_T, \bar{n}_e, P_L)$  was performed. It is well known that the size of the bias in the OLS fits caused by a particular principal component (PC) is equal to the square of the error-to-variance ratio:  $\sim (\lambda_e/\lambda_{pc})^2$ . Here,  $\lambda_{pc}$  is the standard deviation of a PC and  $\lambda_e$  denotes the standard deviation of particular PC due to the errors in engineering variables [13, 14]. Using the errors in engineering variables given above we found that in our case  $(\lambda_e/\lambda_{pc})^2 = [0.067, 0.12, 0.094, 0.12]$ , ordered from the largest to the smallest PC respectively. The PCs are related to engineering variables as  $PC1 \sim n_e^{0.5} P_L^{0.8}$ ,  $PC2 \sim n_e^{0.6}/P_L^{0.6}$ ,  $PC3 \sim I_p^{0.8}/n_e^{0.6}$ ,  $PC4 \sim B_T^{0.9}$ . Thus, the bias of the largest exponent in the OLS fit,  $\alpha_B$ , is  $\sim 12\%$ .

To encapsulate the  $I_p$  and  $B_T$  dependencies further, we have narrowed the dataset to the data representing only  $I_p$  and  $B_T$  scans at high beam power. This analysis is shown in figures 2 and 3. It is seen that these single parameter scans confirm the values found in 4 parameter fits above. The electron energy content  $W_{e,kin}$  shows similar  $I_p$  and  $B_T$  dependences as the total energy content  $W_{mag}$ . In addition  $W_{mag} \approx 2.7 \times W_{e,kin}$  in both scans. This is consistent with the thermal energy content of  $W_{th} \approx 2W_{e,kin} \approx 0.74W_{mag}$  as found in TRANSP analysis for selected data points (see below).

Single parameter scans in figs 2 and 3 revealed that the density range is still not narrow enough. In particular there is a correlation in the  $B_T$  scan: the higher  $B_T$  plasmas tend to have higher densities. To eliminate this we have narrowed the datasets further just to 2-point scans. For each pair the density, power and either  $B_T$  or  $I_p$  were matched as close as possible and then a heat transport analysis was performed. The results are shown in figures 4 and 5. Starting with the  $I_p$  scan, it is seen that there is a slight mismatch in

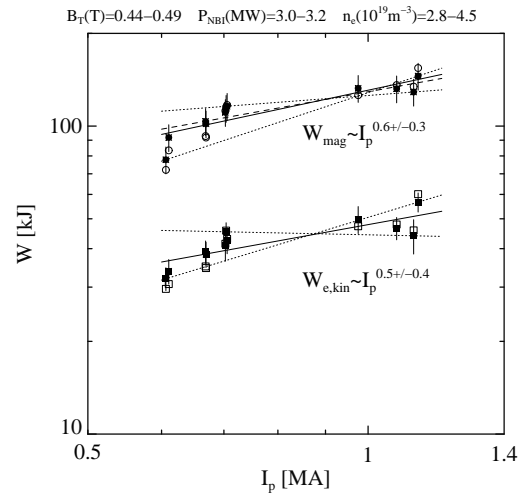


FIG 2. Dependence of total and electron energy contents on plasma current. Full symbols are data corrected for small differences in  $B_T$  assuming  $W \propto B_T^{1.5}$ , open symbols are uncorrected data. The full lines are the regression fits. Dotted lines represent the minimum and maximum possible slopes. The dashed line is  $2.7 \times W_{e,kin,fit}$ . The error bars in the exponents are not statistical errors but the min-max ranges based on extreme cases

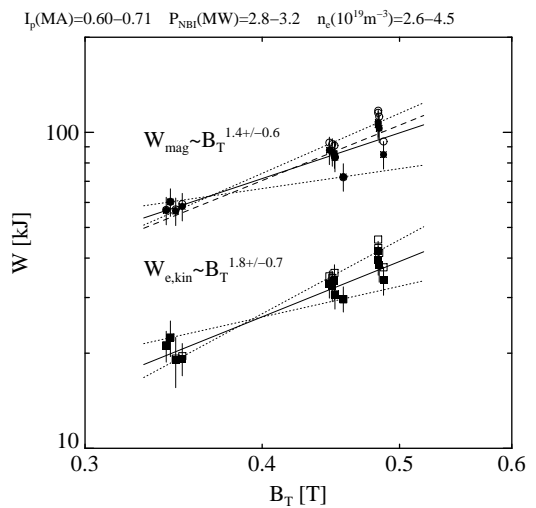


FIG 3. Dependence of total and electron energy contents on toroidal field. The full symbols are data corrected for small differences in  $I_p$  assuming  $W \propto I_p^{0.6}$ , other symbols as in Fig. 2.

Starting with the  $I_p$  scan, it is seen that there is a slight mismatch in

the total heat flux  $q_T$  (figure 4b) as calculated by the TRANSP code. This is caused by different ohmic powers at different  $I_p$ . Taking this into account the electron energy content scales with plasma current as  $W_{e,kin} \propto I_p^{0.63} P_L^{1/3}$  (fig. 4c). This is in agreement with all the above results. The ion temperature  $T_i$  in this scan is measured with a neutral particle analyser and shows that  $T_e \approx T_i$  at mid radius (fig. 4c). Assuming  $T_e \approx T_i$  for all relevant radii we calculate the effective heat diffusivity as  $\chi_{eff} = -q_T/2n_e \nabla T_e$ . (The neo-classical ion heat flux calculated by TRANSP for  $T_i = T_e$  is rather small,  $\sim 20\%$  of  $q_T$ .) Figure 4d shows the ratio of  $\chi_{eff}$  for the  $I_p$  scan. In the outer half of the plasma, the measured ratio cannot be explained by simple gyro-Bohm transport  $\chi_{eff} \propto \chi_{gB}$ . The discrepancy can be reconciled by invoking a dependence on safety factor  $q$  as  $\chi_{eff} \propto \chi_{gB} q$ . This dependence is nevertheless still weaker than in conventional aspect tokamaks where  $\chi_{eff} \propto \chi_{gB} q^{1.5}$  or stronger is measured [15]. This finding is in line with weaker  $I_p$  scaling of global confinement in MAST.

Fig. 5 shows similar analysis for the  $B_T$  scan. Matching the density and power (fig. 5a, b) results in a scaling  $W_{e,kin} \propto B_T^{1.3}$ . This is in line with our previous analyses bearing in mind the possible  $\bar{n}_e - B_T$  interplay. Fig 5d shows that the  $B_T$  scan cannot be explained by the model  $\chi_{eff} \propto \chi_{gB} q$  alone. Agreement can be obtained by adding a collisionality dependence of  $\chi_{eff} \propto \chi_{gB} q \nu_*^{x_{\nu_*}}$  with  $x_{\nu_*} = 2/3$  or even stronger. Here,  $\nu_* \propto n_e/T_e^2$ . For comparison, in conventional tokamaks  $x_{\nu_*} \approx 0.4$  [16]. The  $\nu_*$  exponent could be somewhat lower if dependence on toroidal beta is invoked (fig. 5d). These models are still consistent with the  $I_p$  scan, perhaps indicating a slightly weaker  $q$  dependence than assumed above (fig. 4d).

Stronger  $\nu_*$  and weaker  $q$  dependence of  $\chi_{eff}$  could explain the strong  $B_T$  dependence in engineering parameters scaling. Mapping the dimensionless gyro-

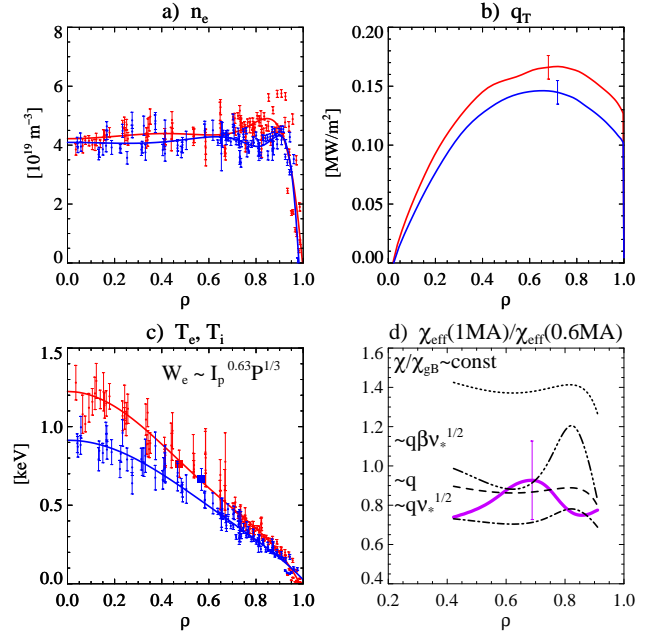


FIG 4. Transport analysis of  $I_p$  scan.  $I_p = 0.97MA$  (red symbols) and  $I_p = 0.61MA$ , (blue symbols).  $B_T = 0.45T$ ,  $\rho = \psi_N^{0.5}$ , where  $\psi_N$  is the normalised poloidal magnetic flux. (b): total heat flux  $q_T$ . (c): symbols with error bars are  $T_e$ , square symbols are  $T_i$  from NPA. (d): pink line is the ratio of experimental diffusivities, black lines are the ratios expected from different models calculated from  $n_e$  and  $T_e$  profiles and with  $q \sim B_T/I_p$ .

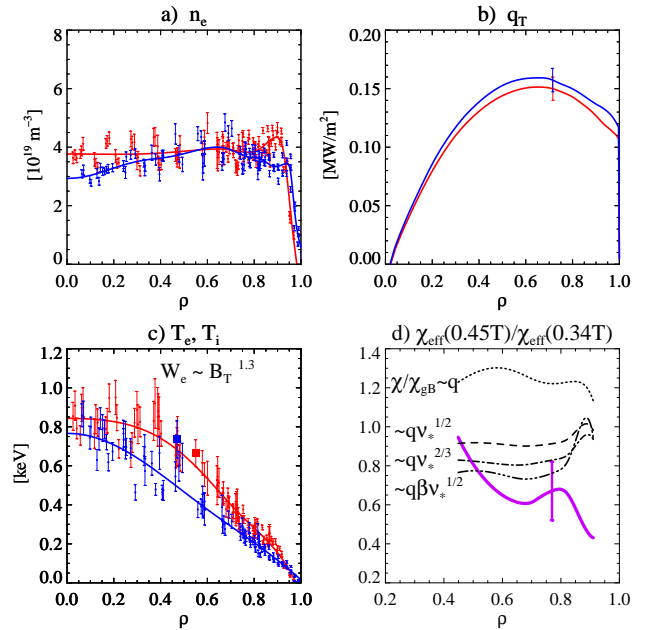


FIG 5. Transport analysis of  $B_T$  scan.  $B_T = 0.45T$  (red symbols) and  $B_T = 0.34T$  (blue symbols).  $I_p = 0.61MA$ . Other notation as in fig. 4.

Bohm scaling  $\tau_E B \propto B/\chi_{eff} \propto \rho_*^{-3} q^{-x_q} \beta^{-x_\beta} \nu_*^{-x_\nu}$  to engineering parameters shows that for  $x_q=1$ , the magnetic field exponent varies from  $\alpha_B=1$  to  $\alpha_B=1.5$  when  $x_{\nu_*}=1/2 \rightarrow 3/4$  and  $x_\beta=0 \rightarrow 1$ . Stronger collisionality dependence is also consistent with the lack of density scaling because  $\alpha_n=0$  for  $x_\nu=1/2$ . Finally, two plasmas from figs. 4 and 5, one with the highest  $I_p$  and one with lowest  $B_T$ , represent approximately a collisionality scan ( $\sim 2\times$ ), which is also consistent with the stronger  $\nu_*$  dependence deduced above.

### 3. Particle confinement

Particle confinement has been studied using deuterium pellets launched from the top and they enter the plasma from the high field side. For more details see [11]. The nominal diameter and length of the cylindrical pellets are  $d_{pel}=L=(1.1;1.35;1.7)mm$  with  $N_{pel}=(0.6;1.2;2.4)\times 10^{20}$  atoms and pellet velocities were in the range of 240-450 m/s. The plasma geometry and heating were the same as for the confinement studies but the plasma current and toroidal field were restricted to  $I_p=(0.66-0.76)MA$ ,  $B_T=(0.47-0.50)T$ . In addition L-mode plasmas were also included. Particle confinement time depends on two processes: (1) the pellet deposition and (2) post-pellet particle transport, each controlled by different physics.

*Pellet deposition.* In MAST, the pellet evaporation and the deposition process is captured by images in the visible and narrow band bremsstrahlung spectrum. The latter reveals clear burst-like structure (striations) of this process and sharp discontinuity in evaporation rate at the end of pellet deposition. Occasionally the pellet trajectories are not straight lines, presumably due to interaction with the neutral beam. This would complicate the pellet deposition analysis and therefore such data are not used in this study. Pellet evaporation lasts about 2 ms and its end is clearly seen on the interferometer signal as a sharp inflexion point. Figure 6 shows the density profiles at the end of evaporation as measured by high spatial resolution ( $\sim 1cm$ ) Thomson scattering triggered directly from the pellet signal with controlled delay. The density profile immediately after pellet evaporation is a combined result of three simultaneous processes: pellet evaporation along the pellet trajectory,  $\nabla B$ -drift of plasmoids which re-deposit particles away from the pellet track, and homogenisation of plasma density over magnetic flux surfaces. Figure 6 compares the measured density profile with those predicted by different models [17]. It is seen that a neutral gas and plasma shielding model (NGPS) [18] without  $\nabla B$ -drift can not explain the observed profile. Good agreement is obtained if NGPS is combined with a first principles  $\nabla B$ -drift model [19]. The model also shows that drift-induced plasma pre-cooling improves the pellet penetration.

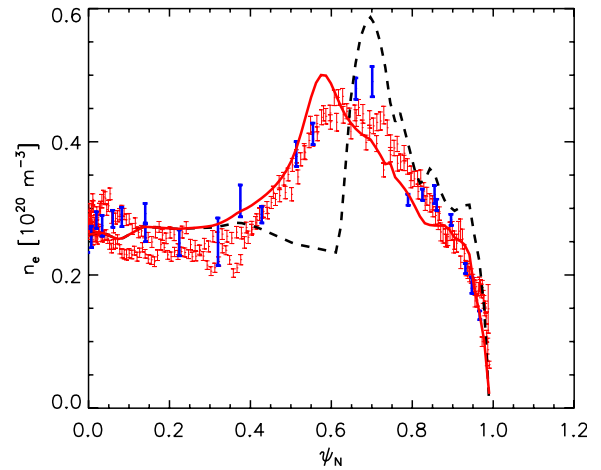


FIG 6. Density profile at the end of pellet deposition. Discrete symbols are the Thomson scattering data, blue and red correspond to different laser systems. Both inboard and outboard profiles are shown. Black dashed line: prediction by NGPS model. Red line: prediction by NGPS model with  $\nabla B$ -drift model [19].

*Post-pellet particle transport.* Soon after pellet deposition and homogenisation the plasma temperature and density are approximately constant on magnetic surfaces as seen from the good overlap of inner and outer profiles when mapped to the poloidal magnetic flux coordinate (see figure 6). This means that the post-pellet particle transport could be studied

using conventional transport models. Figure 7b shows two density profiles, one before and one just after the pellet deposition, as captured by the 200 Hz Thomson scattering system. It is seen that the pellet creates a distinct zone with positive density gradient  $\nabla n_e > 0$  and normalised temperature gradient  $a/L_{Te} \equiv -a\nabla \ln T_e$  doubled relative to its pre-pellet value (see figure 7a). The effect of these changes on the micro-turbulence has been investigated by two turbulence simulation codes: linear GS2 [20] and CUTIE [22]. The analysis is performed for the plasma in figure 7a and 7b and for the flux surface  $\sqrt{\psi_N} \sim 0.7$  where the pellet-induced increase of normalised temperature gradient  $a/L_{Te}$  is maximum. Figure 7c shows the mixing length estimate of diffusivity  $\gamma/k_y^2$  for a range of poloidal wave numbers  $k_y \rho_i$  as calculated by GS2. Here,  $\gamma$  is the linear growth rate,  $\mathbf{k}_y$  is the poloidal wave vector perpendicular to the total magnetic field,  $\rho_i = \sqrt{T_i m_i} / (eB)$  is the ion Larmor radius where  $m_i$  is the ion mass,  $e$  is the electron charge. The ion temperature is  $T_i \approx T_e$ , as measured by charge exchange spectroscopy and a neutral particle analyser. It is seen that the diffusivity  $\gamma/k_y^2$  due to the modes with  $0.08 < k_y \rho_i < 0.8$  increases by a factor of  $\sim 2$  when compared to the pre-pellet case. The modes with longer wavelength are identified as micro-tearing modes while those with shorter wavelength as ion temperature gradient (ITG) modes. The stability of these modes strongly depends on the flow shearing rate  $\omega_{E \times B}$  which, however, is not measured in the pellet case. In the non-pellet case,  $\omega_{E \times B}$  is found to be of the same magnitude as that required to stabilise the long wavelength modes  $\omega_{E \times B} \sim \gamma(k_y \rho_i < 1)$  [21]. The plasma in figures 7a and 7b has also been modelled by the global, fully electromagnetic CUTIE code [22]. It includes all fluid drift-waves (ITG modes, collisional drift waves, tearing and ballooning modes) but it does not include trapped particle physics and does not represent tight-aspect ratio shaped equilibria accurately. In our simulations, boundary conditions for particle and heat transport are introduced by a narrow zone with strong particle and heat sinks to represent the effect of the scrape-off-layer. Such a plasma is deduced to be in H-mode as indicated by a large radial electric field and reduced edge turbulence inside the CUTIE boundary. Figure 7d shows the relative amplitude of the density fluctuations  $\delta n/n$  in the simulation at  $r/a = 0.7$  for a range of wave numbers  $k_\theta \rho_s$ . Here,  $k_\theta$  is the poloidal wave number and  $\rho_s = \sqrt{(T_e + T_i) m_i} / (eB)$  (note  $k_\theta \rho_s$  in CUTIE differs from  $k_y \rho_i$  in GS2). It is seen that the amplitude of fluctuations increases almost threefold for modes with  $0.07 < k_\theta \rho_s < 0.2$  and decreases for modes with  $0.2 < k_\theta \rho_s < 0.4$ , but the overall turbulent transport increases. The modes  $0.07 < k_\theta \rho_s < 0.2$  are identified with the electromagnetic (i.e. drift-Alfvén) branch. The radial extent of these modes is about 2 times smaller than the poloidal extent. The

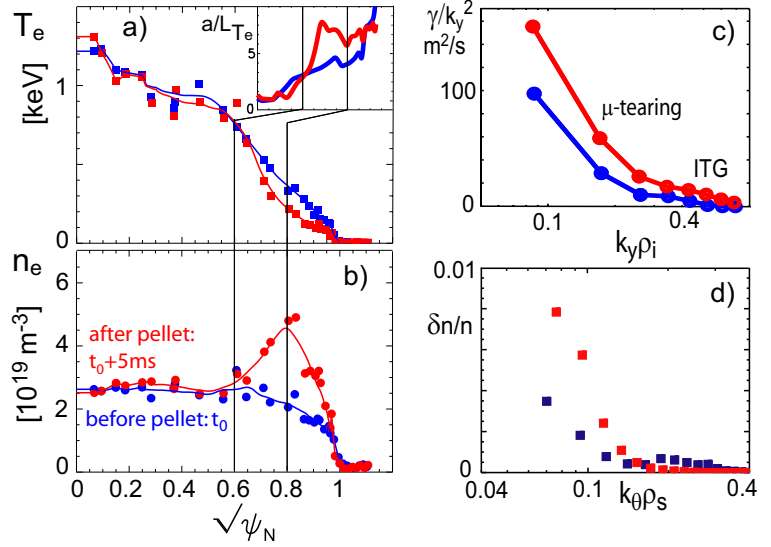


FIG 7. (a, b) Experimental electron temperature,  $T_e$ , and electron density,  $n_e$ , profiles before (blue) and after (red) pellet injection. The insert panel shows the normalised electron temperature gradient  $a/L_{Te}$  over a small range of minor radius as indicated. The plasma is in ELMy H-mode,  $I_p = 0.72 \text{ MA}$ ,  $B_T = 0.50 \text{ T}$  and  $P_{INJ} = 2.0 \text{ MW}$ . (c) Calculated normalised growth rates of micro-turbulence using the linear GS2 code without rotation shear. (d) Simulated amplitudes of density fluctuations of micro-turbulence using the CUTIE code.

temporary increase of particle transport in the zone with  $\nabla n_e > 0$ , as indicated above by both simulations, would result in a further inward particle propagation of pellet material in addition to the  $\nabla \mathbf{B}$ -drift and thus would be favourable for pellet deposition. In addition to this, the distinct zone in which the pellets modify the density and temperature profiles could take-over the role of the pedestal for setting-up the boundary condition for transport in the plasma core in general.

Particle transport in the pellet deposition zone determines the pellet retention time  $\tau_{pel}$  (the life time of the pellet-induced perturbation). In MAST,  $\tau_{pel}$  can be measured directly with the help of the 200Hz Thomson scattering by an exponential fit to the post-pellet evolution of electron density at fixed position  $r = r_{pel}$  [11]. Here,  $r_{pel}$  is the pellet deposition radius (radius of the maximum density perturbation due to the pellet). Figure 8 shows pellet retention time as a function of normalised pellet deposition radius  $\rho_{pel} = r_{pel}/a$ . In order to obtain useful scalings  $\tau_{pel}$  is normalised to the global energy confinement time  $\tau_{E,tot}$ . The energy

confinement time  $\tau_{E,tot}$  includes also fast ions (contribution below 30%). Note that  $\tau_{E,tot}$  is not constant in the dataset but varies by a factor of 2.3 and 1.8 in the L-mode and ELMy H-mode subsets respectively. Two types of correlations are evident from the data in figure 8. Firstly, the pellet retention time decreases rapidly as the pellet deposition becomes shallower. This trend is faster than expected from the diffusion coefficient being independent of minor radius. Secondly, the alignment of L-mode and H-mode points shows that the pellet retention time correlates with the energy confinement time: i.e. L-modes have poorer particle confinement than ELMy H-modes for the same pellet deposition radius.

This correlation of pellet retention with the status of the edge transport barrier means that magnetic ergodisation for ELM mitigation may significantly reduce  $\tau_{pel}$ . Experiments are under way in MAST to investigate this.

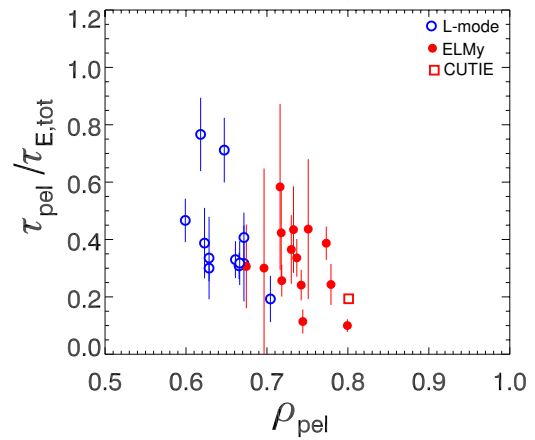


FIG 8. Pellet retention time normalised to global energy confinement time  $\tau_{pel}/\tau_{E,tot}$  plotted against the pellet deposition radius.

#### 4. Discussion

We have shown that the energy confinement time in MAST displays a strong dependence on toroidal magnetic field. This is similar to NSTX [7] data, but in contrast to conventional IPB98(y,2) scaling used so far for predictions towards a Component Test Facility based on the spherical tokamak (ST-CTF) [4]. ST-CTF is aimed to produce 35MW of fusion power with a MAST-size plasma. This is predicted if the normalised thermal energy confinement time is  $H \equiv \tau_{E,th}/\tau_{IPB98,y2} = 1.3$  and engineering parameters are:  $I_p = 6.5MA$ ,  $B_T \sim 2.47T$ ,  $\bar{n}_e = 1.1 \times 10^{20} m^{-3}$ ,  $\kappa = 2.4$ ,  $P_{aux} = 44MW$ . Energy confinement scaling derived from MAST data (table 1, case 1) corrected for fast ion content,  $\tau_{E,th}(s) = 0.74 \times W_{mag,MJ} / P_{L,MW} = 0.186 I_{p,MA}^{0.59} B_T^{1.4} P_{L,MW}^{-0.73}$ , predicts that for ST-CTF the normalised thermal energy confinement time is  $H \sim 1.6$ . Here,  $\kappa$  and effective mass,  $M$ , scaling are taken from IPB98(y,2), though NSTX indicates a weaker  $\kappa$  scaling [8]. For comparison, the scaling derived from NSTX data predicts a normalised energy confinement of  $H \sim 1.8$  (scaling 3, table 1 in [8] with IPB98(y,2)-like  $\kappa$  and  $M$  exponents). These favourable predictions to ST-CTF are the result of the strong  $B_T$  dependence in both the MAST and NSTX scalings. If proved universal, it could allow re-optimisation of the ST-CTF in order to ease the requirements on its most

critical parts such as the divertor and neutral beams. The question of universality of the  $B_T$  scaling is however not trivial. If the strong  $B_T$  dependence is indeed the result of strong  $\nu_*$  scaling, as suggested in this work, then one expects that this dependence will become weaker towards lower  $\nu_*$  values, as observed in conventional tokamaks. Note that  $\nu_*$  is the main dimensionless variable along which the confinement is extrapolated from MAST to ST-CTF [5].

Particle confinement time determines the design of fuelling, pumping and tritium reprocessing systems in fusion reactors. MAST data show that the post-pellet particle confinement time  $\tau_{pel}$  correlates with the status of the edge transport barrier (L-mode or H-mode) and decreases rapidly for pellet deposition radius  $r_{pel}$  approaching the plasma edge. The particle throughput  $\Phi_{pel}$  necessary to maintain the required plasma density is determined by these two parameters as:  $\Phi_{pel} \approx n_e S(a - r_{pel}) / \tau_{pel}$ , where  $S$  is the plasma surface area and  $n_e$  is the time-averaged density in the pellet deposition zone. For pellet deposition expected in ITER,  $r_{pel} \approx 0.80a$  [9], the MAST data in figure 8 extrapolate to  $\tau_{pel} \sim 0.2\tau_E \approx 0.74s$  and the particle throughput is then  $\Phi_{pel} \approx 70Pa m^3 / s$ . Such a value of pellet throughput is about 70% of the original ITER design value for steady state operation [2]. The same estimate for ST-CTF gives a pellet fuelling rate of  $\Phi_{pel} \sim 20Pa m^3 / s$ , i.e. about a quarter of that in ITER. Here, due to the smaller plasma size in CTF we assumed deeper pellet penetration,  $r_{pel} \sim 0.7a$  which from figure 8 gives a pellet retention time of  $\tau_{pel} / \tau_E \sim 0.5$ . The scaling for particle confinement presented here is a first attempt of this sort and clearly needs further refinements. The prediction of  $r_{pel}$  for a burning plasma is difficult due to the uncertainty in  $\nabla B$ -drift. Another uncertainty is the dependence of pellet retention time  $\tau_{pel}$  on aspect ratio, pellet size and pellet frequency  $f_{pel}$ . For example in ITER,  $f_{pel} \sim 6Hz$ . This is about four times faster than  $1/\tau_{pel}$  which is rare in present experiments. In addition, all techniques suggested to mitigate the ELM size lead to a reduction of particle confinement at the edge causing density pump-out. In devices such as ITER and ST-CTF this has to be compensated by an additional increase of pellet particle throughput in order to control plasma density at the required value. Finally, the pellet deposition zone could setup the effective core boundary and thus modify the confinement.

**Acknowledgement.** This work was funded jointly by the United Kingdom Engineering and Physical Sciences Research Council and by the European Communities under the contract of Association between EURATOM and UKAEA. The views and opinions expressed herein do not necessarily reflect those of the European Commission.

- [1] ITER Physics Basis, Nucl. Fusion **39** (1999) 2204
- [2] ITER Final Design Report 2001, [http://www.iter.org/a/index\\_nav4.htm](http://www.iter.org/a/index_nav4.htm)
- [3] MAISONNIER, D. et al., Nucl. Fusion **47** (2007) 1524
- [4] VOSS, G. et al., Fusion Eng. Design (2008) doi:10.1016/j.fusengdes.2008.05.002
- [5] VALOVIĆ, M. et al., Nucl. Fusion **45** (2005) 942
- [6] KAYE, S. et al., Plasma Phys. Control. Fusion **48** (2006) A429
- [7] KAYE, S. et al., Nucl. Fusion **47** (2007) 499
- [8] KAYE, S. et al., Nucl. Fusion **46** (2006) 848
- [9] POLEVOI, A. et al., Nucl. Fusion **43** (2003) 1072
- [10] BAYLOR, L. et al., Nucl. Fusion **47** (2007) 443
- [11] VALOVIĆ, M. et al., Nucl. Fusion **48** (2008) 075006
- [12] TRANSP code <http://w3.pppl.gov/transp/>
- [13] FULLER, W. A. 1987 Measurement Error Models (New York: Wiley) chapter 4
- [14] CORDEY, J. G. et al., Nucl. Fusion **45** (2005) 1078
- [15] GARBET, X. et al., Plasma Phys. Control. Fusion **46** (2004) 1351
- [16] PETTY, C. C. et al., Plasma Phys. Control. Fusion **46** (2004) A207
- [17] GARZOTTI, L. et al., 35th EPS Conference, 2008, Hersonissos (Greece), O4.054
- [18] GARZOTTI, L. et al., Nucl. Fusion **37** (1997) 1167
- [19] PEGOURIE, B. et al., Nucl. Fusion **47** (2007) 44
- [20] KOTSCHENREUTER, M. et al., Comp. Phys. Comm. **88** (1995)128
- [21] ROACH C. M. et al., Plasma Phys. Control. Fusion **47** (2005) B323
- [22] THYAGARAJA, A. et al., Phys. Plasmas **12** (2005) 090907